Unveiling the oxidation mechanism of persistent organic contaminants via visible light-induced dye-sensitized reaction by red mud suspension with peroxymonosulfate

Joohyun Kim, Jaehyeong Park, Sunho Yoon, Juri Lee, Khalil Hanna, Jaesang Lee, Changha Lee, Jong Kwon Choe, Sungjun Bae

Highlights

- A novel dye-sensitized oxidation system was developed by utilizing RM and PMS
- Amorphous FeO(OH)/α-Fe_2O_3 in RM played a crucial role in the enhanced PMS activation
- Photo-sensitized AO7* enhanced the electron transfer in the Fe^{III}/Fe^{II} cycle
- Oxidized dye and $^1O_2$ played an additional role in the enhanced PMS activation
- AO7/RM/PMS/vis system exhibits notable reusability and applicability in water samples

Unveiling the oxidation mechanism of persistent organic contaminants via visible light-induced dye-sensitized reaction by red mud suspension with peroxymonosulfate

Joohyun Kim[a,b], Jaehyeong Park[c], Sunho Yoon[a], Juri Lee[b], Khalil Hanna[d], Jaesang Lee[e], Changha Lee[b], Jong Kwon Choe[c], and Sungjun Bae[a,*]

[a]*Department of Civil and Environmental Engineering, Konkuk University, 120 Neungdong-ro, Gwangjin-gu, Seoul 05029, Republic of Korea*

[b]*School of Chemical and Biological Engineering, Institute of Chemical Process (ICP), and Institute of Engineering Research, Seoul National University, 1 Gwanak-ro, Gwanak-gu, Seoul 08826, Republic of Korea*

[c]*Department of Civil and Environmental Engineering and Institute of Construction and Environmental Engineering, Seoul National University, 1 Gwanak-ro Gwanak-gu, Seoul 08826, Republic of Korea*

[d]*Univ. Rennes, Ecole Nationale Supérieure de Chimie de Rennes, CNRS, ISCR-UMR 6226, F-35000 Rennes, France*

[e]*Civil, Environmental, and Architectural Engineering, Korea University, Seoul 136-701, Republic of Korea*

*Corresponding author: bsj1003@konkuk.ac.kr

phone: +82-42-450-3904

A revised manuscript submitted to Water Research

January, 2024

Abstract

A dye-sensitized photocatalysis system was developed for degrading persistent organic contaminants using solid waste (i.e., red mud, RM) and peroxymonosulfate (PMS) under visible light. Complete degradation of acid orange 7 (AO7) was achieved in RM suspension with PMS, where the co-existence of amorphous FeO(OH)/α-Fe_2O_3 was the key factor for PMS activation. The experimental results obtained from photochemical and electrochemical observations confirmed the enhanced PMS activation due to the Fe-OH phase in RM. DFT calculations verified the acceleration of PMS activation due to the high adsorption energy of PMS on FeO(OH) and low energy barrier for generating reactive radicals. Compared to the control experiment without AO7 showing almost no degradation of other organic contaminants (phenol, bisphenol A, 4-chlorophenol, 4-nitrophenol, and benzoic acid), photo-sensitized AO7* enhanced electron transfer in the Fe^{III}/Fe^{II} cycle, dramatically enhancing the degradation of organic contaminants via radical ($^{\bullet}OH$, $SO_4^{\bullet-}$, and $O_2^{\bullet-}$) and non-radical ((dye^{*+}) and $^1O_2$) pathways. Therefore, the novel finding of this study can provide new insights for unique PMS activation by heterogeneous Fe(III) containing solid wastes and highlight the importance of sensitized dye on the interaction of PMS with Fe charge carrier for the photo-oxidation of organic contaminants under visible light.

Keywords: Red mud; Acid orange 7; Peroxymonosulfate; organic contaminants; Photo-oxidation

1. Introduction

Recently, various advanced oxidation processes (AOPs) have been extensively studied for the effective decomposition and mineralization of persistent pollutants in municipal and industrial wastewater [1–3]. Most conventional AOPs rely on the formation of the hydroxyl radical ($^{\bullet}OH$), which is highly reactive and nonselective in the oxidization of various organic contaminants. Recently, sulfate radical ($SO_4^{\bullet-}$)-based AOPs have attracted attention as effective processes for wastewater treatment owing to the comparatively high redox potential of $SO_4^{\bullet-}$ (2.5–3.1 V vs. NHE) and selectivity over a wide pH range compared to $^{\bullet}OH$ (1.8–2.7 V vs NHE) [4]. In numerous previous studies, peroxymonosulfate (PMS) has been used to produce $SO_4^{\bullet-}$ for the oxidation of organic contaminants [5–9]. PMS can be activated by direct photolysis, electrolysis, or by metals in the reduced state (e.g., Fe(0), Co^{2+}, Cu^{+}, and Fe^{2+}) because PMS undergoes heterolytic peroxide bond dissociation to yield $SO_4^{\bullet-}$ via radical pathways [7,10]. Various Fe-containing minerals such as hematite (α-Fe_2O_3), goethite (α-FeOOH), and pyrite (FeS_2) also show good efficiency for PMS activation [11,12]. Furthermore, singlet oxygen ($^1O_2$), which is a highly selective oxidant, can be produced by the uncatalyzed self-decay of PMS under alkaline conditions (one of the known nonradical pathways) [7].

Red mud (RM) is a solid waste generated in the Bayer process for alumina production by the alkaline extraction of bauxite ore. Because of the large quantity, high alkalinity, and corrosivity of RM, the management of RM is considered a major environmental issue worldwide [13,14]. Over the past decades, most of the generated RM has been disposed in landfill sites, resulting in potential soil contamination and groundwater pollution [15,16]. Therefore, many researchers have developed sustainable techniques of utilizing RM. The utilization of RM as a construction and building material is the most common and efficient method of recycling RM on a large scale [17–19]. Various applications of RM have been

investigated including the recovery of valuable elements, as an adsorbent for heavy metal removal, and as a catalyst or support material for environmental remediation [20–24]. Because RM comprises nanosized particles composed mostly of Fe species (e.g., α-Fe_2O_3 and FeO(OH)), it has a potential application in heterogeneous AOPs for the degradation of persistent pollutants. Li et al. achieved enhanced degradation of sulfamethoxazole using the Fe_3O_4/FeO(OH)/PMS system owing to the electron transfer from Fe_3O_4 to FeO(OH) and surface oxygen vacancies of FeO(OH), resulting in efficient PMS activation [25]. However, α-Fe_2O_3 (i.e., Fe(III) mineral) in RM could not transfer an electron to vicinal FeO(OH), which limits the utility of RM in PMS activation for the effective removal of various organic contaminants.

Utilization of reducing agents and photochemical grafting are promising solutions for improving the efficiency of the Fe(III)-containing catalyzed systems for PMS activation. Many studies have reported that the addition of Fe-reductants (e.g., ascorbic acid, protocatechuic acid and hydroxylamine) can accelerate the Fe(III)/Fe(II) redox cycle, resulting in greatly enhanced PMS activation [26–29]. However, residual amounts of reducing agents or their by-products may remain in treated water and pose a risk to aquatic ecosystems. By contrast, photocatalysis is a sustainable and eco-friendly approach for utilizing energy, especially visible light. Much attention has been paid to visible light-induced PMS activation by nonmetal and metal doping, as well as dye-sensitization in Fe_2O_3-catalyzed systems [30–35]. Among these strategies, dye-sensitized system refers to the process of electron transfer from a photoexcited dye to an electron acceptor, which is a promising solution for overcoming the limitations of Fe-containing catalyzed PMS activation. However, previous studies reporting on the dye-sensitized PMS activation employing Fe containing solid wastes have focused only on the utilization of reduced Fe species (i.e., Fe^0 and Fe_3O_4) [36,37], and have encountered the

limitations in the utilization of Fe(III) materials, which constitutes a significant portion in Fe containing solid wastes and natural minerals [13,38,39]. In addition, simultaneous degradation of persistent contaminants by dye-sensitized PMS activation systems has been rarely discussed; with focusing solely on the decolorization of the dye itself.

This study investigates a visible light-induced photocatalytic system for PMS activation using RM (RM/PMS/vis) in the presence of acid orange 7 (AO7, photosensitizer) for enhanced oxidation of AO7 and other organic pollutants (e.g., phenol, bisphenol A (BPA), 4-chlorophenol (4-CP), 4-nitrophenol (4-NP), furfuryl alcohol (FFA) and benzoic acid (BA)). The objectives of this study were i) to characterize the raw RM, other RM-mimicking materials and neutralized RM (NRM), ii) to investigate the removal kinetics of AO7 by RM/PMS/vis system , iii) to elucidate the enhanced oxidation and sensitization mechanism of AO7 by RM/PMS/vis system via experimental and theoretical investigations including density functional theory (DFT) calculations, iv) to find out the most crucial mineral phase and reactive site in RM, and v) to investigate the AO7-sensitized oxidation of various persistent organic contaminants and governing degradation mechanism.

2. Materials and Methods

2.1. Chemicals

All chemicals were of reagent grade and used without further purification. AO7, PMS (Oxone®), *tert*-butanol (*t*-BuOH), 2-propanol (2-PrOH), superoxide dismutase from bovine erythrocytes (SOD), 5,5-dimethyl-1-pyrroline *N*-oxide (DMPO), iron(III) oxide (Fe_2O_3), sodium oxide (80%, Na_2O), calcium oxide (CaO), titanium(IV) oxide (anatase, TiO_2), silicon dioxide (SiO_2), aluminum oxide (Al_2O_3), Nafion® perfluorinated resin solution (Nafion), ethanol, *p*-hydroxyphenylacetic acid, horseradish peroxidase, potassium hydrogen phthalate,

sodium sulfate (Na_2SO_4), potassium bromate ($KBrO_3$), phenol, BPA, 4-CP, 4-NP, FFA, BA, crystal violet (1% aqueous solution, CV), rhodamine B (RhB), and reactive black 5 (RB5) were purchased from Sigma–Aldrich. Sodium hydroxide (NaOH), hydrochloric acid (37%, HCl), and phosphoric acid were provided by Dae Jung Chemical Company. Acetonitrile (HPLC grade) was purchased from J.T. Baker. Deionized water (DIW, 18.2 MΩ·cm, Millipore Milli-Q Integral 5) was used to prepare all solutions in this study.

2.2. Preparation and characterization of the materials

Raw RM produced from the Bayer process was obtained from the Korea Institute of Geoscience and Mineral Resources in Daejeon, South Korea. Before its use, raw RM was dried at 105 °C in a drying oven and ground uniformly using a mortar and pestle. To investigate the effect of the surface hydroxyl groups in RM, neutralized RM (NRM) was prepared by acid treatment. To neutralize RM, 0.5 M HCl was added dropwise to the RM suspension (5 g of RM in 500 mL DIW; the initial pH of the suspension was ~ 13) under continuous stirring until the pH reached 7. Thereafter, NRM was separated by vacuum filtration and washed with DIW and dried at 105 °C in a dry oven. To examine the role of the metal oxides comprising RM for PMS activation, RM-mimicking metal oxide composites were prepared by a hydrothermal method. Various composites were prepared by adding different metal oxides to Fe_2O_3 based on the chemical composition of RM (Table S1): Fe_2O_3 (37.3%)−Al_2O_3 (23.7%), −TiO_2 (6.7%), −CaO (5.4%), −SiO_2 (10.4%), and −Na_2O (5.5%). First, 5 g of metal oxide mixture was added to 100 mL of DIW and vigorously mixed for 2 h. The suspension was transferred to a Teflon-lined autoclave and heated at 180 ℃ for 12 h. Finally, the suspension was dried at 105 ℃ for 24 h. The prepared composites of Fe_2O_3−Al_2O_3, −TiO_2, −CaO, −SiO_2, and −Na_2O are denoted as FeAl, FeTi, FeCa, FeSi, and FeNa, respectively. The composite of all the metal oxides is

donated as a synthesized RM (SRM). To investigate the effect of the alkalinity of the materials, Fe_2O_3 (37.3%)−Na_2O (1%) and −Na_2O (3%) were prepared, which are denoted as FeNa-1 and FeNa-3, respectively.

The morphology and particle size of RM was investigated by transmission electron microscopy equipped with energy dispersive spectroscopy (TEM-EDS; JEM-2010, JEOL). The chemical composition and mineral phase of the materials were identified by X-ray fluorescence (XRF; XRF-1700, Shimadzu) and X-ray diffraction (XRD; JP/MAX-3C, Rigaku), respectively. The oxidation state of Fe in RM was monitored by X-ray photoelectron spectroscopy (XPS; Axis-Supra, Kratos) and X-ray absorption near-edge spectroscopy (XANES; R-XAS, Rigaku). Fourier-transform infrared (FTIR) spectra of the materials used in this study were acquired by the ATR method, over the range of 4000–650 cm^{-1} (Magna 860, Nicolet).

2.3 Experimental procedure for photochemical reaction

AO7 and the organic contaminants (i.e., phenol, BPA, 4-CP, 4-NP, FFA and BA) were subjected to photochemical oxidation in a quartz reactor containing 100 mL of the suspension of the prepared materials (catalysts) with PMS. For kinetics experiments, 0.1 g/L (or the desired amount of the materials) was completely dispersed by ultrasonication. To initiate the reaction, PMS was injected into the suspension to obtain an initial concentration of 4 mM, followed by irradiation with visible light using a 150 W xenon lamp equipped with a long-pass optical filter ($\lambda > 400$ nm). The initial pH of the reaction solution was maintained at 3.0 by injecting the PMS reagents, and the pH changed only marginally over the reaction. For the control experiments without PMS addition, the initial pH was adjusted to the same value with 0.1 M HCl. One mL of aliquot was withdrawn at predetermined time intervals and filtered through a

0.2 μm PTFE syringe filter. For the experiments in natural waters, three different water samples (i.e., tap water, river water, and groundwater) were collected in the Republic of Korea; river water and groundwater were collected at the Han River and South Chungcheong province, respectively. The water samples were immediately filtered using 0.45 μm nylon filter and stored at 4℃ until use. All kinetics experiments were conducted in duplicate and showed good reproducibility; the average values with standard deviations are presented.

2.4 Photochemical and electrochemical analyses

Photoluminescence (PL) spectra were recorded using a fluorescence spectrophotometer (F-7100, Hitachi Co.) with excitation at 400 nm. The electrochemical characteristics of RM were analyzed using a potentiostat (VSP, BioLogic Co.) under visible light irradiation ($\lambda > 400$ nm, 100 mW/cm^2). For the photocurrent measurement, the photo-generated current on the materials was monitored in a three-electrode cell containing a 0.1 M Na_2SO_4 electrolyte; the open circuit potential was recorded in chronoamperometric mode under light on and off conditions. Electrochemical impedance spectroscopy (EIS) analysis was performed within the frequency range of 0.1 Hz to 100 kHz at an alternating current voltage amplitude of 10 mV. For the photocurrent and EIS measurements, the material (catalyst)-coated glass, Pt mesh, and Ag/AgCl were used as the working, counter, and reference electrodes, respectively. To prepare the working electrode, the catalyst suspension was prepared by dispersing 10 mg catalyst in ethanol containing 10% (v/v) Nafion as a binding agent. Thereafter, 50 μL of the suspension was dropped and spread on the surface of an indium tin oxide-coated glass (ITO glass; 1 cm × 1 cm; 15–25 Ω/square). To immobilize the catalyst, the resulting catalyst-coated ITO glass was dried at 80 ℃ for 30 min.

2.5 Analytical methods

To monitor the kinetics of AO7 degradation, 0.5 mL of sample was transferred to the cuvette containing 1 mL of DIW to determine the concentration of AO7 using a UV-vis spectrophotometer (Lambda 465, PerkinElmer) at 484 nm. Other organic contaminants were analyzed by ultrahigh performance liquid chromatography (UHPLC) with a UV-vis detector (UltiMate 3000, Thermo Scientific) equipped with an Acclaim 120 C18 column. A mixture of 0.1% (v/v) aqueous phosphoric acid solution and acetonitrile (80:20 ratio by volume) was used as the mobile phase [40]. The total organic carbon (TOC) was measured using a TOC analyzer (Sievers M5310 C). To identify the intermediates in the degradation of AO7, LC-QTOF-MS analysis was performed using a high-pressure LC instrument (Ultimate3000, Thermo Scientific Inc., USA) coupled to an AB Sciex TripleTOF 5600 + system (AB Sciex, USA) with a C18 column. The eluents used as the mobile phase were prepared from a mixture of 0.1% formic acid in water and 0.1% formic acid in acetonitrile. Direct evidence of radical generation in the RM/PMS/vis system was obtained by electron spin resonance (ESR, JES-X310, JEOL) analysis. The concentration of dissolved ions in the water samples was determined by ion chromatography (Metrohm, Eco IC). The suspension containing 100 mM of DMPO, 0.1g/L of RM, and 4 mM of PMS was injected into the ESR cell and analyzed under visible light irradiation. ESR analysis was performed at a resonance frequency of 9.45 GHz, microwave power of 0.998 mW, modulation frequency of 100 kHz, modulation amplitude of 1.0 G, sweep width of 1.0 G, time constant of 30 ms, and sweep time of 30 s. The in situ generated H_2O_2 was measured using a fluorescence probe [41,42]. The signals were obtained on a fluorescence spectrophotometer (F-7100, Hitachi Co.) with excitation and emission wavelengths of 315 and 406 nm, respectively.

2.6 DFT calculations

To investigate the oxidative pathway of AO7, DFT calculation was performed using ORCA 5.0.3 [43]. The initial geometry and input file for AO7 and the transformation product (TP) were prepared using the Avogadro program [44]. The geometry of AO7 and the intermediates was optimized using the B3LYP method with the 6-31G(d, p) basis set and D3-BJ [45]. All calculations were accelerated using the RIJCOSX algorithm. To consider the solvation effect, the conductor-like polarizable continuum model (CPCM) was employed for aqueous systems. In addition, the reactive sites of AO7 and its intermediates were forecasted using the Fukui function, a recognized technique for predicting the regioselectivity in radical-involving reactions [46–48]. The Fukui function and f^{-}_{A} are defined as follows [49]:

$$f(r) = \left[\frac{\partial \rho(r)}{\partial N}\right]_{\nu} \quad (1)$$

$$f^{-}_{A} = q_A(N) - q_A(N-1) \quad (2)$$

The electron density at point r is described as $\rho(r)$, where N is the total number of electrons and the constant term ν in the partial derivative is the external potential. The condensed Fukui function was estimated using the Hirshfeld charge number, which is the distribution of the electron density around the atom [46]. $q_A(N)$ and $q_A(N-1)$ refer to the atomic charge states of atom A in the presence of N and $N-1$ electrons, respectively. This concept becomes important in understanding how certain atoms undergo preferential electrophilic attack, described by the f^{-} values [47,50]. All visualizations and graphics were prepared using ChemCraft (1.8 version).

To compare the adsorption and transition state energies of the materials and the PMS molecule, all geometry optimizations were performed using VASP (version 6). The GGA-PBE exchange-correlation functional, RMM-DIIS algorithm, and real space projection operators were used in a plane-wave basis set with a cutoff at 400 eV. For structure optimization, the unit-cells were optimized first; a = 7.4 and b = 5.4 Å for Fe_2O_3, a = 6.3 and b =7.7 Å for

FeO(OH). The space in the c-direction (25 Å) is far enough to ignore the interaction between supercells next to each other. To calculate the adsorption energy, the unit-cells were expanded by (2 × 2 × 1), and the bottom two layers were frozen in vacuum conditions. The iron atom on the Fe_2O_3 and FeO(OH) lattices and three different oxygen atoms of PMS were selected as adsorption sites; the oxygen atoms in the O–O bond and sulfate group of PMS were labeled as O_1, O_2, and O_3, respectively. The energy for the adsorption of PMS on both the Fe_2O_3 and FeO(OH) surfaces was calculated as follows [51]:

$$E_{\text{adsoprtion}} = E_{\text{PMS-surface}} - (E_{\text{PMS}} + E_{\text{surface}}) \quad (3)$$

For the transition state search, the O_3-adsorbed surface, which has the lowest energy, was used in the unit cell. The transition state was optimized using elastic band methods.

3. Results and Discussion

3.1. Characterization of raw RM and synthetic catalysts

The morphological and structural characteristics of raw RM were identified by TEM-EDS analysis (Fig. 1(a) and Fig. S1(a)), which showed an irregular nanosized RM agglomerate composed of various elements (i.e., Fe, Si, Ca, Al, Ti, and Na). EDS mapping also revealed that Fe and Al are the main elements, which is in good agreement with the XRF data (37.3% of Fe and 23.7% of Al as oxide; Table S1). The Fe2p XPS and XANES Fe K-edge spectra of RM were similar to those of Fe_2O_3 (Fig. S2(a) and (b)). An XRD analysis of RM (Fig. 1(b)) revealed that RM is composed of various mineral phases such as hematite (α-Fe_2O_3), boehmite (γ-AlO(OH)), anatase (TiO_2), calcite ($CaCO_3$), and quartz (SiO_2), as previously reported [52,53]. In addition, the (012), (104), and (110) planes of Fe_2O_3 in RM were confirmed based on the electron diffraction patterns (Fig. S1(b–d)), with the estimated d-spacing values of 0.37, 0.27, and 0.252 nm, respectively [54]. FeNa and SRM prepared by a process similar to the

preparation of RM comprised similar mineral phases, mainly α-Fe_2O_3. FTIR and XPS analyses also confirmed the presence of FeO(OH) on the RM surface. The FTIR spectra exhibited distinct bands at 880, 1629, and 3420 cm^{-1}, ascribed to Fe−O−H bending, −OH bending, and −OH stretching vibrations, respectively (Fig. 1(c)); all these bands are related to hydroxyl groups [55,56]. A comparison of Fe_2O_3 and the RM-mimicking materials (i.e., FeNa and SRM) showed an increase in the number of hydroxyl groups in the RM-mimicking materials. In comparison, the band at 880 cm^{-1} disappeared in the spectrum of NRM, further confirming the presence of FeO(OH) in RM. The O1s XPS profiles of the materials (Fig. 1(d)) were deconvoluted into peaks at 531.4 (Fe-OH) and 529.6 eV (Fe-O), where the Fe-O peak of Fe_2O_3 was dominant. Compared to the case of Fe_2O_3, the peak corresponding to Fe-OH significantly increased in the alkali-treated materials (i.e., FeNa, SRM, and raw RM). The Fe-OH peak of NRM also slightly decreased compared to RM. Based on the results of XRD, FTIR, and XPS, we can confirm that FeO(OH) is present in its amorphous form in RM, not crystalline α-FeO(OH) (goethite) and γ-FeO(OH) (lepidocrocite).

3.2. Degradation of AO7 by the RM/PMS/vis system

3.2.1 Degradation kinetics of AO7

The high amount of Fe species in RM led to the design of a novel dye-sensitized PMS activation system for the simultaneous degradation of dyes and other organic contaminants. First, AO7 was chosen as a model dye contaminant because it forms a strong complex with α-Fe_2O_3 [35] and is commonly detected in textile wastewater [57]. Under dark conditions, PMS alone was ineffective for removing AO7, whereas very low removal (≤ 5%) of AO7 was observed in both RM and RM/PMS systems (Fig. 2(a)). This finding indicates insignificant adsorption of AO7 on the RM surface and inability of RM to activate PMS. Under visible light

irradiation, the RM/vis system also showed no significant effect on AO7 removal (Fig. 2(b)), indicating that the RM/vis system cannot induce PMS activation, plausibly owing to the fast electron-hole recombination in this system, despite the suitable band-gap energy (1.81 eV) for excitation (Fig. S3). PMS/vis induced slight degradation of AO7 (17% of AO7 in 120 min). Because many studies have shown a negligible effect of visible irradiation for direct PMS activation [58,59], it is theorized that visible light-sensitized AO7 ($AO7^*$) is formed, which can slowly activate PMS to generate ROS. Compared with the control experiments, the visible light-activated RM/PMS system (RM/PMS/vis) induced a dramatic increase in the degradation of AO7 (Fig. 2(b)): 97% degradation in 100 min under 1-sun condition. The intensity of the original bands in the UV-vis spectra at 484 and 430 nm (corresponding to hydrazone and azo forms, respectively) continuously decreased as the irradiation time increased (Fig. S4). The absorbance of the naphthalene and benzene rings (i.e., 310 and 228 nm) also decreased during the reaction, indicating that further degradation to intermediates occurred after the decolorization of AO7 [60].

3.2.2 Reactive oxygen species for AO7 degradation

To identify the ROS responsible for AO7 degradation in the RM/PMS/vis system, the effects of dissolved oxygen (anoxic condition) and different additives (i.e., *t*-BuOH, 2-PrOH, and FFA) were examined (Fig. 2(c) and (e)); dissolved oxygen is responsible for the generation of $O_2^{\bullet-}$, FFA is a $^1O_2$ probe ($k_{1_{O_2}}$ = 1.2 × 10^8 M^{-1} s^{-1}), *t*-BuOH is a specific $^{\bullet}OH$ scavenger ($k_{\bullet OH}$ = 3.8 – 7.6 × 10^8 M^{-1} s^{-1}), and 2-PrOH can scavenge both $^{\bullet}OH$ and $SO_4^{\bullet-}$ ($k_{\bullet OH}$ = 1.9 × 10^9 and $k_{SO_4^{\bullet-}}$ = 4–7.42 × 10^7 M^{-1} s^{-1}) [61,62]. The addition of *t*-BuOH slightly inhibited AO7 degradation, delaying complete removal by 10 min (Fig. 2(c)). By contrast, excess 2-PrOH significantly inhibited the degradation rate to less than 30% in 120 min. These results indicate

that the reactive oxidants (i.e., $^{\bullet}OH$ and $SO_4^{\bullet-}$) were generated by the RM/PMS/vis system, and $SO_4^{\bullet-}$ was mainly responsible for AO7 degradation, rather than $^{\bullet}OH$. ESR analysis after irradiation clearly indicated that the production of DMPO-OH and DMPO-SO_4 adducts increased as the reaction time increased (Fig. 2(d)). Under anoxic conditions, the kinetics of AO7 degradation by RM/PMS/vis were severely delayed (53% removal in 120 min), indicating that $O_2^{\bullet-}$ plays an important role in AO7 degradation. In this system, it is believed that a major role of $O_2^{\bullet-}$ is to activate PMS, leading to the generation of $^{\bullet}OH$ and $SO_4^{\bullet-}$, rather than the direct oxidation of AO7. This explanation is supported by the following experimental results. First, the generation of $O_2^{\bullet-}$ in the AO7/vis and AO7/RM/vis systems without PMS was measured based on the H_2O_2 production in a mixture with SOD (Fig. S5) [63]. Despite a remarkable increase in the H_2O_2 production in both systems, no degradation of AO7 was observed in either of the aforementioned systems (denoted as vis alone and RM/vis in Fig 2(b)). These results suggest that direct oxidation of AO7 by $O_2^{\bullet-}$ is of marginal importance in the RM/PMS/vis system. Conversely, in the PMS/vis system, the apparent degradation of AO7 was 17% within 120 min, indicating that the $O_2^{\bullet-}$ generated by electron transfer from AO7* to O_2 plays a key role in the activation of PMS. In addition, the effect of $O_2^{\bullet-}$ on PMS activation increased in the presence of RM because a larger amount of $O_2^{\bullet-}$ was generated (1.8-fold enhancement; Fig. S5). Note that the data suggest that another pathway for PMS activation through a substantial contribution of RM is strongly likely because the degradation of AO7 was not completely inhibited by deoxygenation; a more detailed discussion is presented in Section 3.3. FFA was minimally degraded by AO7/vis and AO7/RM/vis, indicating that the amount of singlet oxygen derived from $O_2^{\bullet-}$ was negligible (Fig. 2(e)). By contrast, significant degradation of FFA was observed in the RM/PMS system under dark conditions, suggesting that $^1O_2$ can be produced by PMS self-decay on the surface of RM from which OH^- is slowly

eluted. The pH of the suspension first increased and then decreased in the RM/PMS system, whereas that of the RM suspension increased continuously. However, $^1O_2$ is not an important reactive oxidant for the degradation of AO7 because no AO7 degradation was achieved in the RM/PMS system (Fig. 2(a)).

3.2.3 Characterization of by-product and degradation pathway of AO7

To identify the oxidative degradation pathway of AO7, the intermediates generated by the RM/PMS/vis system were analyzed using LC-QTOF-MS. During the reaction, eleven different TPs were identified with good certainty (mass errors < 5 ppm). The proposed oxidative degradation pathways for AO7 are summarized in Fig. 3(a); the mass-to-charge ratio (*m/z*) of all TPs is indicated in the nomenclature (e.g., TP327). The MS/MS spectra of the oxidation intermediates are also provided in Fig. S6. In the initial stage of degradation, hydroxylated products of AO7 such as TP361, TP377, and TP393 were identified. After hydroxylation, further ring cleavage products containing benzenesulfonate and naphthalene were detected. In the further oxidative degradation, TP172 sequentially underwent denitrification, hydroxylation (TP188), and desulfonation (TP109); contrastingly, the ring opening of naphthalene proceeded through TP191, TP147, TP179, TP149, and TP109.

Additional DFT calculations were performed to support the degradation pathway of AO7 in this study; the hydroxylated products of AO7 (i.e., TP361, TP377, and TP393) were computationally specified by Fukui functions. The chemical structures with a condensed Fukui function for electrophilic attack (i.e., $f-$ values) are presented in Fig. 3(b); a site with a high $f-$ value is highly vulnerable to electrophilic attack (oxidative attack). For AO7 (TP327), the highest $f-$ values were identified for the azo bonds of N_{11} (0.0790) and N_{12} (0.0993), indicating that the first step is the cleavage of the azo bonds to a single bond by hydroxylation (i.e.,

TP361). Thereafter, C_1 and C_7 of TP361 with high $f-$ values of 0.0593 and 0.0564, respectively, are expected to be sequentially hydroxylated.

3.3. Role of metal oxides in RM

To identify the role of metal oxides in RM, the four most abundant metal oxides in RM (i.e., 0.1 g/L of Fe_2O_3, Al_2O_3, SiO_2, and TiO_2) were used for AO7 degradation in the presence of PMS under visible light (Fig. 4(a)). As shown earlier, PMS alone afforded 17% removal, which is similar to that achieved with TiO_2 (i.e., 23% degradation of AO7 in 120 min). By contrast, Fe_2O_3 afforded remarkably higher AO7 removal, i.e., 65% removal in 120 min, whereas Al_2O_3 and SiO_2 completely inhibited the degradation of AO7. These results suggest that the Fe component in RM is mainly responsible for PMS activation, leading to enhanced generation of ROS in the RM/PMS/vis system. By contrast, Al_2O_3 and SiO_2 can prevent the reduction of O_2 to $O_2^{\bullet-}$ by scavenging the electrons from $AO7^*$.

The synergistic effects of the complexation of the RM components were examined using RM-mimicking materials (i.e., FeAl, FeTi, FeCa, FeSi, FeNa, and SRM); the determined amount of the materials, as much as included in 0.1 g/L RM based on chemical composition (Table S1), was used for AO7 degradation (Fig. 4(b)). With FeAl and FeSi, almost no AO7 was removed within 4 h, which is consistent with the results obtained with single metal oxides. Compared to the control experiment (Fe_2O_3), FeTi and FeCa exerted inhibitory effects on AO7 removal: 45%, 22%, and 29% of AO7 was removed in 4 h with 37 mg/L of Fe_2O_3, 44 mg/L of FeTi, and 43 mg/L of FeCa, respectively. These results indicate that the Al, Si, Ti, and Ca components can hinder adsorption of the adsorbates (i.e., AO7 and PMS) on Fe_2O_3 through competitive occupation of the active sites, thereby inhibiting electron transfer from AO7 to PMS. By contrast, FeNa exhibited significantly higher AO7 removal (complete removal within

100 min), and SRM also had a faster removal rate compared with that of Fe_2O_3; however, the removal rate achieved with SRM was lower than that obtained with FeNa, possibly due to the inhibitory effect of the components (Al, Si, Ti, and Ca). These results support the key role of the Fe component of RM in AO7 degradation. FeNa and SRM, prepared in highly alkaline conditions, contained amorphous FeO(OH)), which can significantly accelerate PMS activation; further details are presented in Section 3.4.

Direct evidence of the role of the Fe component was obtained by XANES analysis for pristine RM and visible light irradiated RM in the presence of AO7 (Fig. 4(c)). The XANES spectra showed peaks corresponding to the Fe K-edge peak (1s → 4p) and pre-edge shoulder (1s → 3d), which are known to correlate with the oxidation state [64–66]. In comparison with pristine RM, a negative shift and lower intensity of the 1s → 4p peak were observed in RM after irradiation, while the intensity of the 1s → 3d peak simultaneously increased. These changes are consistent with the difference between Fe_3O_4 and Fe_2O_3, indicating that the Fe(III) contained in RM was reduced to Fe(II) by electron transfer from $AO7^*$.

3.4 Enhanced PMS activation by FeO(OH) in RM

3.4.1 Kinetics of AO7 degradation

To investigate the enhanced kinetics of AO7 degradation by FeO(OH) in RM, the effects of the Na_2O content during synthesis and NRM on AO7 degradation were evaluated (Fig. 5(a) and (b)). FeNa-3 (3%) and FeNa (5.5%) afforded drastically higher removal efficiencies (removing more than 90% of AO7 within 70 min), whereas the removal efficient of FeNa-1 was only slightly higher than that of Fe_2O_3. This difference indicates that the rate of AO7 degradation increased drastically as the Na_2O content increased. Compared to pristine RM, the rate of AO7 degradation decreased significantly with NRM (70% removal in 120 min),

possibly due to the low amount of amorphous FeO(OH), as indicated by the FTIR and XPS data (Fig. 5(b)). These results suggest that the presence of FeO(OH)/α-Fe_2O_3 in RM leads to improved degradation efficiency.

3.4.2 Photochemical and electrochemical analyses

The enhancement of PMS activation by FeO(OH) can also be explained by the photochemical and electrochemical analyses (i.e., PL analysis and photocurrent and EIS measurements) of FeO(OH)-rich (i.e., FeNa and RM) and -poor materials (i.e., Fe_2O_3 and NRM). For all tested materials, the current was immediately responsive to the light on and off conditions in the presence of AO7 (Fig. 5(c)), indicating successful electron transfer and capture from the sensitized AO7* to the materials. The photocurrent density obtained with the FeO(OH)-rich materials was much higher than that obtained with the FeO(OH)-poor materials, i.e., an approximately 4- and 8-fold increase in FeNa and RM, respectively, compared to Fe_2O_3 and NRM. This difference indicates that FeO(OH) significantly enhances Fe-mediated PMS activation via dye-sensitized electron transfer. To identify the enhancement of electron mobility between AO7 and FeO(OH), EIS measurements were conducted for the materials under visible light (Fig. 5(d)). The inset image shows the equivalent circuit of the Nyquist plot consisting of the electrolyte resistance (*Rs*), charge transfer resistance (*Rct*), and capacitive phase element (CPE). The obtained resistance for the FeO(OH)-rich materials was lower than that of the FeO(OH)-poor materials, indicating more active electron mobility from AO7 to FeO(OH) in the former. The PL emission peaks for the RM-based (i.e., RM and NRM) and RM-mimicking materials (i.e., Fe_2O_3 and FeNa) were observed at 584 and 598 nm, respectively (Fig. 5(e)). The intensity followed the order: RM < NRM and FeNa < Fe_2O_3, indicating that the FeO(OH)-rich materials exhibited superior efficiency for charge separation. These photochemical and

electrochemical observations explain the enhanced PMS activation due to the FeO(OH) phase in RM.

3.4.3 DFT calculations of adsorption energy and energy barrier

To understand the mechanism of acceleration of PMS activation by the FeO(OH) phase, the adsorption energies of PMS on the Fe_2O_3 and FeO(OH) surfaces were obtained using DFT calculations. The calculated adsorption energies of PMS on Fe_2O_3 and FeO(OH) with three different oxygen atoms (O1–3 in PMS; Fig. S7) and the length of the O–O bond are presented as average values in Table 1. The adsorption energy of PMS on the FeO(OH) is −2.32 eV, which is lower than that on the Fe_2O_3 of −1.40 eV, and all results calculated for each site were in good agreement with the order Fe_2O_3 > FeO(OH). The lower adsorption energy on the FeO(OH) surface suggests a more stable absorption of the PMS molecule compared to the Fe_2O_3 surface. In addition, it is conceivable that catalyzed charge transfer from FeO(OH) would be more efficient due to the stronger interaction with PMS. Meanwhile, the length of the O–O bond in PMS was slightly extended to 1.462 Å and 1.465 Å in Fe_2O_3 and FeO(OH), respectively compared to that (1.460 Å) of free PMS, suggesting that PMS might be easily to cleaved to form $^{\bullet}OH$ and $SO_4^{\bullet-}$ [67,68]. Since the O–O bond of PMS adsorbed on FeO(OH) is longer than that adsorbed on Fe_2O_3, these observations also support that the efficiency of PMS activation by FeO(OH) is superior to that of Fe_2O_3. Moreover, the energy barrier for free radical generation was examined via transition state calculation (Fig. 6). The transition state energy of FeO(OH) was 2.91 eV, which is lower than that of Fe_2O_3 (4.13 eV), demonstrating that the existence of the hydroxyl group makes it easier to overcome energy barrier for PMS activation. The relative energy of the products (decomposition state) for Fe_2O_3 and FeO(OH) (0.22 and 0.51 eV, respectively) was higher than that of the reactants (adsorption state), indicating that

PMS activation on the materials was not thermodynamically spontaneous. However, radical generation is an exergonic reaction from the transition to decomposition state, which can occur with external energy (photon energy in this study).

3.5 Dye-sensitized oxidation of persistent organic contaminants

3.5.1 Degradation of persistent organic contaminants

The PMS-activated degradation and mineralization of phenol with and without AO7 were examined (Fig. 7(a)). In the absence of AO7 (RM/PMS/vis), phenol degradation was negligible (< 5%), whereas phenol completely degraded when the reaction was performed in the presence of AO7 (AO7/RM/PMS/vis) for 3 h. After the initiation of AO7 decolorization, phenol was sequentially decomposed, and almost 40% of the organic contaminants, including AO7, was mineralized (Fig. 7(a)). For the remaining organic contaminants (i.e., BPA, 4-CP, 4-NP, FFA, and BA), the degradation efficiency of the three systems (i.e., RM/PMS/vis, AO7/PMS/vis, and AO7/RM/PMS/vis) was evaluated (Fig. 7(b)); refer to Fig. S8 for degradation kinetics curves. Compared to both the RM/PMS/vis and AO7/PMS/vis systems, significant improvements were observed in degradation efficiency in the presence of AO7 and RM (AO7/RM/PMS/vis) for all contaminants. Phenol, BPA, and 4-CP exhibited degradation rates of 99.9%, 79%, and 70%, respectively, within 3 h in the AO7/RM/PMS/vis system, whereas the RM/PMS/vis and AO7/PMS/vis systems achieved only approximately 10% removal of each contaminant over the same reaction time. Although 4-NP and BA exhibited lower efficiencies, achieving 60% and 40% degradation, compared with other phenolic contaminants, a noticeable improvement was evident in the AO7/RM/PMS/vis system. The dye-sensitized RM/PMS/vis achieved complete degradation of FFA, and the former two systems also showed relatively high efficiency compared to other contaminants due to its high rate constant with $^1O_2$ (Table S2).

3.5.2 Reusability test

The reusability of RM for the simultaneous degradation of AO7 and phenol in the AO7/RM/PMS/vis system was evaluated in seven consecutive reaction cycles (Fig. 7(c)). The used RM particles were collected by centrifugation and re-dispersed in the solution containing the contaminants. Although the degradation rate decreased slightly with increasing cycle number, complete decolorization of AO7 and more than 90% degradation of phenol were achieved simultaneously over 4 h in each of the five cycles. In the 6th cycle, AO7 did not undergo complete decolorization within the desired time, and the degradation rate of phenol also decreased to 75%; a slightly lower degradation rate was observed in the 7th cycle. The decrease in the catalytic activity may be attributed to a reduction in the hydroxyl groups, and the number of active sites due to the remaining residue of organic contaminants on the surface; the small amount of RM usage and loss of RM during the reuse processes may also be responsible for the decrease.

3.5.3 Effect of the dye type

To identify the effect of the dye type on PMS activation, four different dyes (i.e., CV, RhB, MO, and RB5) were used for dye-sensitized phenol oxidation (Fig. 7(d)). For all dyes, the production of $^{\bullet}OH$ or $SO_4^{\bullet-}$ through PMS activation was increased by RM, as confirmed by ESR analysis (Fig. 8). Compared to the absence of the dye, the addition of 50 μM CV and RhB induced a slight increase in the phenol degradation rate to 20%. Notably, the addition of RB5 and AO7 induced significant improvements in the phenol degradation to 70% and 99%, respectively, within the same reaction time. The remarkable increase in efficiency by RB5 and AO7 can be attributed to the presence of azo (–N=N–), hydroxyl (–OH), and sulfonate ($–SO_3^-$)

groups [35,69].These groups are known to form strong complexes with $Fe(OH)_2^+$ under acidic conditions, resulting in the origin of efficient charge transfer; especially, azo and hydroxyl groups of the dye act as an electron donor [69,70].

3.5.4 Effect of RM concentration and water matrices

To optimize the experimental condition, the degradation and mineralization efficiency of phenol was evaluated with different concentrations of RM in the AO7/RM/PMS/vis system. In the presence of 50 μM AO7, a complete degradation of phenol was observed within 4 h using 0.1 g/L of RM as a catalyst (Fig. 9 (a)). As increase in RM concentration up to 0.3 g/L, we observed a significant improvement of phenol degradation, while 0.5 g/L of RM showed a substantial inhibition in degradation kinetics. Meanwhile, the TOC removal rate after one-day reaction in the AO7/RM/PMS/vis system exhibited an increasing trend as the RM concentration increased from 0.1 to 0.3 g/L (62% and 88%, respectively), and the mineralization efficiency of 0.5 g/L RM was a similar level to that of 0.3 g/L RM (Fig. 9 (b)). The obtained results suggest that optimal degradation kinetics and mineralization efficiency can be achieved by using 0.3 g/L RM in the AO7/RM/PMS/vis system. To evaluate the applicability of the AO7/RM/PMS/vis system in different water matrices, the effect of water samples (i.e., tap water, river water, and groundwater) on the degradation efficiency of phenol was examined (Fig. 9 (c)), Compared to the control experiment (i.e., DIW), the degradation kinetics of phenol was decreased in all water samples; and in the order of groundwater < river water < tap water < DIW. These results indicate that the presence of organic and inorganic constituents (Table S3) cause inhibitory effect on the degradation of organic contaminants by hindering the catalytic reaction [71,72]; however, more than 95% of phenol was still decomposed within 4 h.

3.6 Degradation mechanism of organic contaminants by dye-sensitized RM/PMS/vis system

Based on the study results, the degradation mechanism of contaminants by the dye-sensitized RM/PMS/vis system is summarized in Fig. 10. Under visible light irradiation, the FeO(OH)/α-Fe_2O_3 in RM served as an efficient electron acceptor and mediator for dye* owing to the formation of a strong complex. This electron transfer mechanism led to the reduction of Fe(III) and O_2 to Fe(II) and $O_2^{\bullet-}$, respectively, and PMS was activated by the reduced species resulting in the generation of $SO_4^{\bullet-}$ and $^{\bullet}OH$. These reactive oxidants constitute the major route for the simultaneous degradation of dye and other contaminants via radical pathway; experimental results demonstrating the scavenging effect on phenol degradation are presented in Fig. S9. In this process, Al_2O_3 and SiO_2 can inhibit charge transfer by blocking active sites and quenching the electrons. Meanwhile, oxidized dye (dye^{*+}) and $^1O_2$ were also generated by nonradical pathways to degrade organic contaminants. To identify the effect of dye^{*+} on the degradation of contaminants, AO7, $KBrO_3$, and phenol were used as a sensitizer, electron quencher, and target contaminant, respectively [73]. Remarkably, 18% of the phenol was degraded by the AO7/RM/$KBrO_3$/vis system, whereas no degradation was observed in the absence of RM (AO7/$KBrO_3$/vis) (Fig. S10). These results indicate that the direct oxidation by dye^{*+} is responsible for the degradation of contaminants, and this process is notably enhanced by the presence of RM. In addition, $^1O_2$ can be generated by the self-decay of PMS, attributed to the continuous release of OH^- from RM surface, and it acts as a selective oxidizing species for the degradation of contaminants. Consequently, in the dye-sensitized RM/PMS/vis system, various organic contaminants including the selected dye undergo effective degradation through the action of reactive oxidants generated by both radical and nonradical pathways.

4. Conclusions

In this study, we first developed a dye-sensitized RM/PMS/vis system for effective oxidation of persistent organic contaminants and demonstrated the mechanism of PMS activation. Experimental results revealed that the degradation kinetics of AO7 dramatically increased using RM as a Fe catalyst in the presence of PMS under visible light. The positive effect of Fe components (i.e., co-existence of amorphous FeO(OH) and α-Fe_2O_3) in RM on PMS activation was confirmed by various experiments utilizing RM-mimicking, FeO(OH)-rich and -poor materials: (i) degradation kinetics of AO7; (ii) photochemical and electrochemical properties confirmed by photocurrent density, EIS, and PL analyses; and (iii) computational calculations of adsorption energy and energy barrier for PMS activation. The oxidative degradation of organic contaminants by the RM/PMS/vis system was significantly enhanced in the presence of AO7 via complex actions of multiple species generated by radical (i.e., $^{\bullet}OH$, $SO_4^{\bullet-}$, and $O_2^{\bullet-}$) and nonradical (i.e., $^1O_2$ and dye^{*+}) pathways. Furthermore, the good reusability and applicability of the dye/RM/PMS/vis system were confirmed through consecutive cycles of contaminant degradation and the oxidative degradation in the different water samples.

From this study, we demonstrated dye-sensitized reaction could be modified in the developed RM/PMS/vis system for enhanced degradation of persistent organic contaminants, and the novel findings of this study can provide new insights for effective PMS activation by heterogeneous Fe(III) containing solid wastes.

Acknowledgments

This work was supported by the National Research Foundation of Korea (NRF) grant funded by the Korean Government (MSIT) (No. 2022R1A2C2005791) and Human Resources Development Program of the Korea Institute of Energy Technology Evaluation and

Planning(KETEP) grant funded by the Ministry of Trade, Industry and Energy, Republic of Korea (No. RS-2023-00237035).

Author contributions

Joohyun Kim: Data curation; Formal analysis; Investigation; Methodology; Validation; Writing - original draft; Writing - review & editing, Jaehyeong Park: Data curation; Methodology; Visualization, Sunho Yoon: Data curation; Investigation, Juri Lee: Data curation; Investigation, Khalil Hanna: Conceptualization, Writing - review & editing, Jaesang Lee: Conceptualization, Writing - original draft, Changha Lee: Writing - review & editing, Jong Kwon Choe: Writing - review & editing, and Sungjun Bae: Conceptualization; Funding acquisition; Project administration; Supervision; Writing - original draft; Writing - review & editing

Data statement

To foster transparency, please state the availability of your data in your submission if your data is unavailable to access or unsuitable to post.

References

[1] Y. Deng, R. Zhao, Advanced Oxidation Processes (AOPs) in Wastewater Treatment, Curr. Pollut. Rep. 1 (2015) 167–176. https://doi.org/10.1007/s40726-015-0015-z.

[2] H. Zheng, Y. Pan, X. Xiang, Oxidation of acidic dye Eosin Y by the solar photo-Fenton processes, J. Hazard. Mater. 141 (2007) 457–464. https://doi.org/10.1016/j.jhazmat.2006.12.018.

[3] S.S. Hutagalung, I. Muchlis, K. Khotimah, Textile Wastewater Treatment using Advanced Oxidation Process (AOP), IOP Conf. Ser.: Mater. Sci. Eng. 722 (2020) 012032. https://doi.org/10.1088/1757-899X/722/1/012032.

[4] X. Chen, W. Wang, H. Xiao, C. Hong, F. Zhu, Y. Yao, Z. Xue, Accelerated TiO_2 photocatalytic degradation of Acid Orange 7 under visible light mediated by peroxymonosulfate, Chem. Eng. J. 193–194 (2012) 290–295. https://doi.org/10.1016/j.cej.2012.04.033.

[5] Q. Yang, Y. Ma, F. Chen, F. Yao, J. Sun, S. Wang, K. Yi, L. Hou, X. Li, D. Wang, Recent advances in photo-activated sulfate radical-advanced oxidation process (SR-AOP) for refractory organic pollutants removal in water, Chem. Eng. J. 378 (2019) 122149. https://doi.org/10.1016/j.cej.2019.122149.

[6] L. Xu, R. Yuan, Y. Guo, D. Xiao, Y. Cao, Z. Wang, J. Liu, Sulfate radical-induced degradation of 2,4,6-trichlorophenol: A de novo formation of chlorinated compounds, Chem. Eng. J. 217 (2013) 169–173. https://doi.org/10.1016/j.cej.2012.11.112.

[7] J. Lee, U. Von Gunten, J.H. Kim, Persulfate-Based Advanced Oxidation: Critical Assessment of Opportunities and Roadblocks, Environ. Sci. Technol. 54 (2020) 3064–3081. https://doi.org/10.1021/acs.est.9b07082.

[8] S. Yang, Y. Shi, X. Wang, Y. Liu, Y. Ren, W. Li, H. Zhang, X. Dai, W. Sun, B. Lai,

Selective elimination of sulfonamide antibiotics upon periodate/catechol process: Dominance of quinone intermediates, Water Res. 242 (2023) https://doi.org/10.1016/j.watres.2023.120317.

[9] A. Wang, P. Zhou, D. Tian, H. Zhang, Z. Xiong, Y. Du, C. He, Y. Yuan, T. Chen, Y. Liu, B. Lai, Enhanced oxidation of fluoroquinolones by visible light-induced peroxydisulfate: The significance of excited triplet state species, Appl. Catal. B. 316 (2022) https://doi.org/10.1016/j.apcatb.2022.121631.

[10] J. Wang, S. Wang, Activation of persulfate (PS) and peroxymonosulfate (PMS) and application for the degradation of emerging contaminants, Chem. Eng. J. 334 (2018) 1502–1517. https://doi.org/10.1016/j.cej.2017.11.059.

[11] Y. Wang, Y. Gao, L. Chen, H. Zhang, Goethite as an efficient heterogeneous Fenton catalyst for the degradation of methyl orange, Catal. Today. 252 (2015) 107–112. https://doi.org/10.1016/j.cattod.2015.01.012.

[12] Y. Feng, H. Li, L. Lin, L. Kong, X. yan Li, D. Wu, H. Zhao, K. Shih, Degradation of 1,4-dioxane via controlled generation of radicals by pyrite-activated oxidants: Synergistic effects, role of disulfides, and activation sites, Chem. Eng. J. 336 (2018) 416–426. https://doi.org/10.1016/j.cej.2017.12.011.

[13] E. Mukiza, L.L. Zhang, X. Liu, N. Zhang, Utilization of red mud in road base and subgrade materials: A review, Resour. Conserv. Recycl. 141 (2019) 187–199. https://doi.org/10.1016/j.resconrec.2018.10.031.

[14] R. Milačič, T. Zuliani, J. Ščančar, Environmental impact of toxic elements in red mud studied by fractionation and speciation procedures, Sci. Total Environ. 426 (2012) 359–365. https://doi.org/10.1016/j.scitotenv.2012.03.080.

[15] M. Economou-Eliopoulos, R. Frei, I. Megremi, Potential leaching of Cr(VI) from

laterite mines and residues of metallurgical products (red mud and slag): An integrated approach, J. Geochem. Explor. 162 (2016) 40–49. https://doi.org/10.1016/j.gexplo.2015.12.007.

[16] A. Anton, M. Rékási, N. Uzinger, G. Széplábi, A. Makó, Modelling the potential effects of the hungarian red mud disaster on soil properties, Water Air Soil Pollut. 223 (2012) 5175–5188. https://doi.org/10.1007/s11270-012-1269-3.

[17] Z. Liu, H. Li, Metallurgical process for valuable elements recovery from red mud - A review, Hydrometallurgy. 155 (2015) 29–43. https://doi.org/10.1016/j.hydromet.2015.03.018.

[18] M.S.S. Lima, L.P. Thives, V. Haritonovs, K. Bajars, Red mud application in construction industry: Review of benefits and possibilities, IOP Conf. Ser.: Mater. Sci. Eng. 251 (2017) 012033. https://doi.org/10.1088/1757-899X/251/1/012033.

[19] J. Yang, B. Xiao, Development of unsintered construction materials from red mud wastes produced in the sintering alumina process, Constr. Build. Mater. 22 (2008) 2299–2307. https://doi.org/10.1016/j.conbuildmat.2007.10.005.

[20] X. Pan, H. Wu, Z. Lv, H. Yu, G. Tu, Recovery of valuable metals from red mud: A comprehensive review, Sci. Total Environ. 904 (2023). https://doi.org/10.1016/j.scitotenv.2023.166686.

[21] Y. Li, J. Wang, Z. Luan, Z. Liang, Arsenic removal from aqueous solution using ferrous based red mud sludge, J. Hazard. Mater. 177 (2010) 131–137. https://doi.org/10.1016/j.jhazmat.2009.12.006.

[22] A.A.S. Oliveira, I.F. Teixeira, T. Christofani, J.C. Tristão, I.R. Guimarães, F.C.C. Moura, Biphasic oxidation reactions promoted by amphiphilic catalysts based on red mud residue, Appl. Catal. B. 144 (2014) 144–151.

https://doi.org/10.1016/j.apcatb.2013.07.015.

[23] H. Li, B. Xu, F. Qi, D. Sun, Z. Chen, Degradation of bezafibrate in wastewater by catalytic ozonation with cobalt doped red mud: Efficiency, intermediates and toxicity, Appl. Catal. B. 152–153 (2014) 342–351. https://doi.org/10.1016/j.apcatb.2014.01.058.

[24] J. Kim, G.N. Coulibaly, S. Yoon, A.A. Assadi, K. Hanna, S. Bae, Red mud-activated peroxymonosulfate process for the removal of fluoroquinolones in hospital wastewater, Water Res. 184 (2020) 116171. https://doi.org/10.1016/j.watres.2020.116171.

[25] C. Li, J. Wu, W. Peng, Z. Fang, J. Liu, Peroxymonosulfate activation for efficient sulfamethoxazole degradation by Fe_3O_4/β-FeOOH nanocomposites: Coexistence of radical and non-radical reactions, Chem. Eng. J. 356 (2019) 904–914. https://doi.org/10.1016/j.cej.2018.09.064.

[26] Y.T. Lin, C. Liang, C.W. Yu, Trichloroethylene Degradation by Various Forms of Iron Activated Persulfate Oxidation with or without the Assistance of Ascorbic Acid, Ind. Eng. Chem. Res. 55 (2016) 2302–2308. https://doi.org/10.1021/acs.iecr.5b04352.

[27] Y. Qin, F. Song, Z. Ai, P. Zhang, L. Zhang, Protocatechuic Acid Promoted Alachlor Degradation in Fe(III)/H_2O_2 Fenton System, Environ. Sci. Technol. 49 (2015) 7948–7956. https://doi.org/10.1021/es506110w.

[28] W. Sang, Z. Li, M. Huang, X. Wu, D. Li, L. Mei, J. Cui, Enhanced transition metal oxide based peroxymonosulfate activation by hydroxylamine for the degradation of sulfamethoxazole, Chem. Eng. J. 383 (2020). https://doi.org/10.1016/j.cej.2019.123057.

[29] J. Zhang, M. Chen, L. Zhu, Activation of peroxymonosulfate by iron-based catalysts for orange G degradation: Role of hydroxylamine, RSC Adv. 6 (2016) 47562–47569. https://doi.org/10.1039/c6ra07231c.

[30] M. Sayed, B. Ren, A.M. Ali, A. Al-Anazi, M.N. Nadagouda, A.A. Ismail, D.D.

Dionysiou, Solar light induced photocatalytic activation of peroxymonosulfate by ultra-thin Ti^{3+} self-doped Fe_2O_3/TiO_2 nanoflakes for the degradation of naphthalene, Appl. Catal. B. 315 (2022). https://doi.org/10.1016/j.apcatb.2022.121532.

[31] X. Zhang, J. Duan, Y. Tan, Y. Deng, C. Li, Z. Sun, Insight into peroxymonosulfate assisted photocatalysis over Fe_2O_3 modified TiO_2/diatomite composite for highly efficient removal of ciprofloxacin, Sep. Purif. Technol. 293 (2022). https://doi.org/10.1016/j.seppur.2022.121123.

[32] N.T.T. Nguyen, A.Q.K. Nguyen, M.S. Kim, C. Lee, S. Kim, J. Kim, Degradation of aqueous organic pollutants using an Fe_2O_3/WO_3 composite photocatalyst as a magnetically separable peroxymonosulfate activator, Sep. Purif. Technol. 267 (2021). https://doi.org/10.1016/j.seppur.2021.118610.

[33] M. Wang, S. Li, J. Kang, Y. Tang, J. Wang, Z. Xu, J. Liu, Enhanced tetracycline degradation by N - C codoped Fe_2O_3 with rich oxygen vacancies in peroxymonosulfate assisting photoelectrochemical oxidation system: performance, mechanism and degradation pathway, Chem. Eng. J. 451 (2023). https://doi.org/10.1016/j.cej.2022.138611.

[34] J. Liu, Y. Zhang, Y. Dong, Z. Jiang, L. Zhang, W. Liu, J. Guan, H. Lin, Highly efficient photo-degradation for tetracycline elimination in pharmaceutical wastewater by α-Fe_2O_3/V_2O_5/BC assisted peroxymonosulfate activation, Sep. Purif. Technol. 328 (2024) 125034. https://doi.org/10.1016/j.seppur.2023.125034.

[35] H. Park, W. Choi, Visible light and Fe(III)-mediated degradation of Acid Orange 7 in the absence of H_2O_2, J. Photochem. Photobiol. A Chem. 159 (2003) 241–247. https://doi.org/10.1016/S1010-6030(03)00141-2.

[36] T. Wen, Y. Zhao, L. Chen, Y. Miao, Z. Zhang, S. Song, T. Zhang, Utilization of

ferrosilicon from waste carbide slag in enhancing light-driven peroxymonosulfate activation for rapid and clean dyes decolorization, J. Clean. Prod. 414 (2023) 137650. https://doi.org/10.1016/j.jclepro.2023.137650.

[37] Y. Zhang, P. Xiangshi, J. Tian, F. Li, X. Fan, L. Ma, R. Zhang, Synthesis of peroxymonosulfate composite catalyst (Fe0/Fe3O4/biochar) using waterworks sludge and walnut shell for degrading methylene blue, J. Environ. Chem. Eng. 9 (2021). https://doi.org/10.1016/j.jece.2021.106856.

[38] A. Mancini, B. Lothenbach, G. Geng, D. Grolimund, D.F. Sanchez, S.C. Fakra, R. Dähn, B. Wehrli, E. Wieland, Iron speciation in blast furnace slag cements, Cem. Concr. Res. 140 (2021). https://doi.org/10.1016/j.cemconres.2020.106287.

[39] L. Lai, Y. He, H. Zhou, B. Huang, G. Yao, B. Lai, Critical review of natural iron-based minerals used as heterogeneous catalysts in peroxide activation processes: Characteristics, applications and mechanisms, J. Hazard. Mater. 416 (2021). https://doi.org/10.1016/j.jhazmat.2021.125809.

[40] H. Kang, D. Lee, K. Lee, H. Kim, H. Lee, M. Sik, C. Lee, Nonradical activation of peroxymonosulfate by hematite for oxidation of organic compounds : A novel mechanism involving high-valent iron species, Chem. Eng. J. 426 (2021) 130743. https://doi.org/10.1016/j.cej.2021.130743.

[41] A.L. Lazrus, G.L. Kok, J.A. Lind, S.N. Gitlin, B.G. Heikes, R.E. Shetter, Automated Fluorometric Method for Hydrogen Peroxide in Air, Anal. Chem. 58 (1986) 594–597. https://doi.org/10.1021/ac00294a024.

[42] N. Chen, H. Shang, S. Tao, X. Wang, G. Zhan, H. Li, Z. Ai, J. Yang, L. Zhang, Visible Light Driven Organic Pollutants Degradation with Hydrothermally Carbonized Sewage Sludge and Oxalate Via Molecular Oxygen Activation, Environ. Sci. Technol. 52 (2018)

12656–12666. https://doi.org/10.1021/acs.est.8b03882.

[43] F. Neese, The ORCA program system, Wiley Interdiscip. Rev. Comput. Mo.l Sci. 2 (2012) 73–78. https://doi.org/10.1002/wcms.81.

[44] M.D. Hanwell, D.E. Curtis, D.C. Lonie, T. Vandermeersch, E. Zurek, G.R. Hutchison, SOFTWARE Open Access Avogadro: an advanced semantic chemical editor, visualization, and analysis platform, 2012. http://www.jcheminf.com/content/4/1/17.

[45] P.M.W. Gill, B.G. Johnson, J.A. Pople, M.J. Frisch, The performance of the Becke-Lee-Yang-Parr (B-LYP) density functional theory with various basis sets, 1992.

[46] Y. Li, Y. Yang, J. Lei, W. Liu, M. Tong, J. Liang, The degradation pathways of carbamazepine in advanced oxidation process: A mini review coupled with DFT calculation, Sci. Total Environ. 779 (2021). https://doi.org/10.1016/j.scitotenv.2021.146498.

[47] B. De Witte, H. Van Langenhove, K. Hemelsoet, K. Demeestere, P. De Wispelaere, V. Van Speybroeck, J. Dewulf, Levofloxacin ozonation in water: Rate determining process parameters and reaction pathway elucidation, Chemosphere. 76 (2009) 683–689. https://doi.org/10.1016/j.chemosphere.2009.03.048.

[48] M. Ma, L. Chen, J. Zhao, W. Liu, H. Ji, Efficient activation of peroxymonosulfate by hollow cobalt hydroxide for degradation of ibuprofen and theoretical study, Chin. Chem. Lett. 30 (2019) 2191–2195. https://doi.org/10.1016/j.cclet.2019.09.031.

[49] P. Geerlings, F. De Proft, W. Langenaeker, Conceptual density functional theory, Chem. Rev. 103 (2003) 1793–1873. https://doi.org/10.1021/cr990029p.

[50] J. Park, S. Bae, Y. Choi, J.K. Choe, Rh-Pd/TiO_2 as bilateral catalysts for reductive and oxidative degradation of fluorinated pharmaceutical contaminants, Appl. Catal. B. 322 (2023). https://doi.org/10.1016/j.apcatb.2022.122089.

[51] M. Zong, D. Song, X. Zhang, X. Huang, X. Lu, K.M. Rosso, Facet-Dependent Photodegradation of Methylene Blue by Hematite Nanoplates in Visible Light, Environ. Sci. Technol. 55 (2021) 677–688. https://doi.org/10.1021/acs.est.0c05592.

[52] M.K. Sahu, U.K. Sahu, R.K. Patel, Adsorption of safranin-O dye on CO_2 neutralized activated red mud waste: Process modelling, analysis and optimization using statistical design, RSC Adv. 5 (2015) 42294–42304. https://doi.org/10.1039/c5ra03777h.

[53] W. Liu, J. Yang, B. Xiao, Application of Bayer red mud for iron recovery and building material production from alumosilicate residues, J. Hazard. Mater. 161 (2009) 474–478. https://doi.org/10.1016/j.jhazmat.2008.03.122.

[54] E. Chernova, V. Botvin, M. Galstenkova, Y. Mukhortova, D. Wagner, E. Gerasimov, M. Surmeneva, A. Kholkin, R. Surmenev, A Comprehensive Study of Synthesis and Analysis of Anisotropic Iron Oxide and Oxyhydroxide Nanoparticles, Nanomaterials 12 (2022) https://doi.org/10.3390/nano12234321.

[55] L. Mallick, A. Rajput, M.K. Adak, A. Kundu, P. Choudhary, B. Chakraborty, γ-FeO(OH) with multiple surface terminations: Intrinsically active for the electrocatalytic oxygen evolution reaction, Dalton Trans. 51 (2022) 15094–15110. https://doi.org/10.1039/d2dt01860h.

[56] P.K. Raul, R.R. Devi, I.M. Umlong, S. Banerjee, L. Singh, M. Purkait, Removal of fluoride from water using iron oxide-hydroxide nanoparticles, J. Nanosci. Nanotechnol, (2012) 3922–3930. https://doi.org/10.1166/jnn.2012.5870.

[57] M. Greluk, Z. Hubicki, Efficient removal of Acid Orange 7 dye from water using the strongly basic anion exchange resin Amberlite IRA-958, Desalination. 278 (2011) 219–226. https://doi.org/10.1016/j.desal.2011.05.024.

[58] J. Sun, C.H. Shen, J. Guo, H. Guo, Y.F. Yin, X.J. Xu, Z.H. Fei, Z.T. Liu, X.J. Wen, Highly

efficient activation of peroxymonosulfate by Co_3O_4/Bi_2WO_6 p-n heterojunction composites for the degradation of ciprofloxacin under visible light irradiation, J. Colloid Interface Sci. 588 (2021) 19–30. https://doi.org/10.1016/j.jcis.2020.12.043.

[59] Z. Cheng, L. Ling, J. Fang, C. Shang, Visible light-driven g-C_3N_4 peroxymonosulfate activation process for carbamazepine degradation: Activation mechanism and matrix effects, Chemosphere. 286 (2022). https://doi.org/10.1016/j.chemosphere.2021.131906.

[60] L. Duan, B. Sun, M. Wei, S. Luo, F. Pan, A. Xu, X. Li, Catalytic degradation of Acid Orange 7 by manganese oxide octahedral molecular sieves with peroxymonosulfate under visible light irradiation, J. Hazard. Mater. 285 (2015) 356–365. https://doi.org/10.1016/j.jhazmat.2014.12.015.

[61] G. V. Buxton, C.L. Greenstock, W.P. Helman, A.B. Ross, Critical Review of rate constants for reactions of hydrated electrons, hydrogen atoms and hydroxyl radicals ($\cdot OH/\cdot O^-$ in Aqueous Solution, J. Phys. Chem. Ref. Data. 17 (1988) 513–886. https://doi.org/10.1063/1.555805.

[62] A.P. Darmanyan, C.S. Foote, P. Jardon, Interaction of Singlet Oxygen with Peroxy and Acylperoxy Radicals, J. Phys. Chem. 99 (1995) 11854–11859. https://pubs.acs.org/sharingguidelines.

[63] J. Čapek, T. Roušar, Detection of oxidative stress induced by nanomaterials in cells—the roles of reactive oxygen species and glutathione, Molecules. 26 (2021). https://doi.org/10.3390/molecules26164710.

[64] J. Wong, F.W. Lytle, R.P. Messmer, D.H. Maylotte, *K*-edge absorption spectra of selected vanadium compounds, Phys. Rev. B. 30 (1984) 5596. https://doi.org/10.1103/PhysRevB.30.5596

[65] A.J. Berry, H.S.C. O'Neill, K.D. Jayasuriya, S.J. Campbell, G.J. Foran, XANES

calibrations for the oxidation state of iron in a silicate glass, Am. Min. 88 (2003) 967-977. https://doi.org/10.2138/am-2003-0704

[66] A. Corrias, G. Ennas, G. Mountjoy, G. Paschina, An X-ray absorption spectroscopy study of the Fe K edge in nanosized maghemite and in Fe_2O_3-SiO_2 nanocomposites, Phys. Chem. Chem. Phys. 2 (2000) 1045–1050. https://doi.org/10.1039/a908698f.

[67] J. Zhang, B. Jing, Z. Tang, Z. Ao, D. Xia, M. Zhu, S. Wang, Experimental and DFT insights into the visible-light driving metal-free C_3N_5 activated persulfate system for efficient water purification, Appl. Catal. B. 289 (2021). https://doi.org/10.1016/j.apcatb.2021.120023.

[68] B. He, L. Song, Z. Zhao, W. Liu, Y. Zhou, J. Shang, X. Cheng, $CuFe_2O_4$/CuO magnetic nano-composite activates PMS to remove ciprofloxacin: Ecotoxicity and DFT calculation, Chem. Eng. J. 446 (2022) https://doi.org/10.1016/j.cej.2022.137183.

[69] M.E. Belghiti, J. Mouldar, M. Bakasse, Computational study of the interaction between azo dye (RR141) and Hematite α-Fe_2O_3(111) Surface: Density Functional Theory and Molecular Dynamics Simulation, Comput. Theor. Chem. (2023) 114355. https://doi.org/10.1016/j.comptc.2023.114355.

[70] J. Bandara, J.A. Mielczarski, J. Kiwi, 2. Photosensitized degradation of azo dyes on Fe, Ti, and Al oxides. Mechanism of charge transfer during the degradation, Langmuir. 15 (1999) 7680–7687. https://doi.org/10.1021/la990030j.

[71] G.Y. Kim, D. Lee, H.S. Choe, J.M. Park, S. Jeong, E.J. Park, J.W. Lee, C. Lee, J.H. Kim, Yolk–shell-type gold nanosphere-encapsulated mesoporous silica for catalytic oxidation of organic pollutants in the presence of persulfate, Environ. Sci. Nano 9 (2022) 2510-2520. https://doi.org/10.1039/d2en00305h.

[72] R. Ahmadiasl, G. Moussavi, S. Shekoohiyan, F. Razavian, Synthesis of Cu doped TiO_2

nanocatalyst for the enhanced photocatalytic degradation and mineralization of gabapentin under UVA/LED irradiation: Characterization and photocatalytic activity, Catalysts 12 (2022) 1310. https://doi.org/10.3390/catal12111310.

[73] T. Cai, Y. Liu, L. Wang, W. Dong, H. Chen, W. Zeng, X. Xia, G. Zeng, Activation of persulfate by photoexcited dye for antibiotic degradation: Radical and nonradical reactions, Chem. Eng. J. 375 (2019). https://doi.org/10.1016/j.cej.2019.122070.

Tables

Table 1. DFT calculation results of adsorption energies of PMS on Fe_2O_3 and FeO(OH), and the length of O–O bond in PMS before and after being adsorbed on Fe_2O_3 and FeO(OH).

Configurations	**Adsorption energy (eV)**	**Length of O–O bond (Å)**
PMS	-	1.460
PMS on Fe_2O_3	-1.40	1.462
PMS on FeO(OH)	-2.32	1.465

Figures

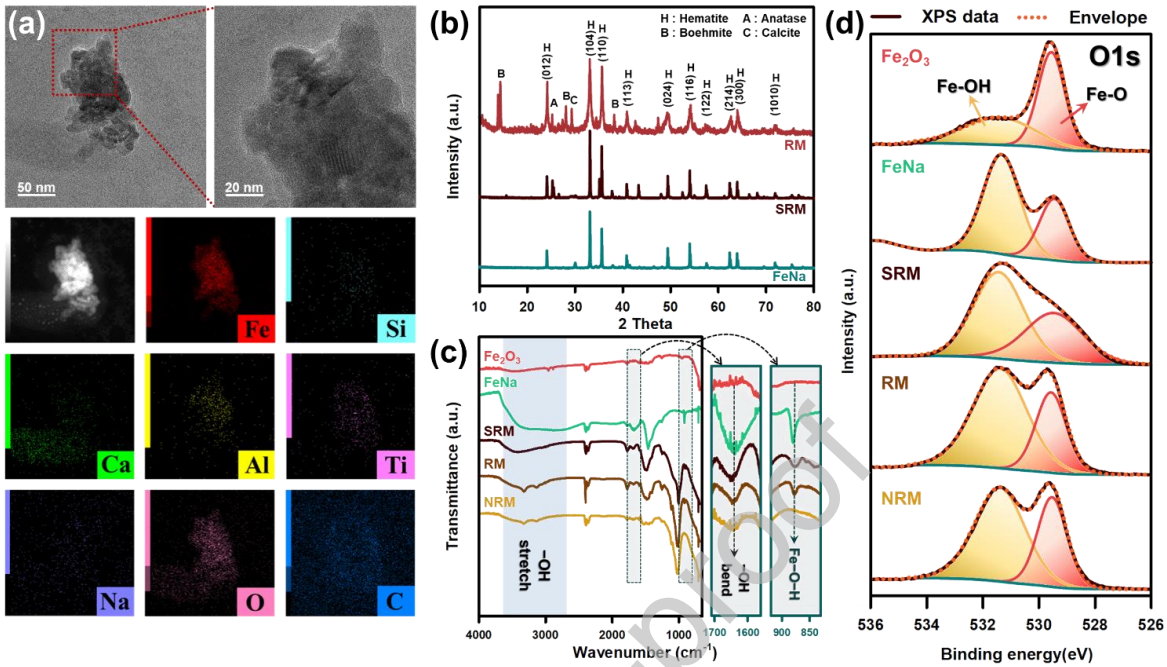

Fig. 1. (a) TEM image of RM with EDS analysis showing the electron mapping of C, O, Na, Al, Si, Ca, Ti, and Fe; (b) XRD pattern of RM, SRM, and FeNa; (c) FTIR spectra and (d) the deconvoluted XPS spectra of O1s for Fe_2O_3, FeNa, SRM, RM, and NRM.

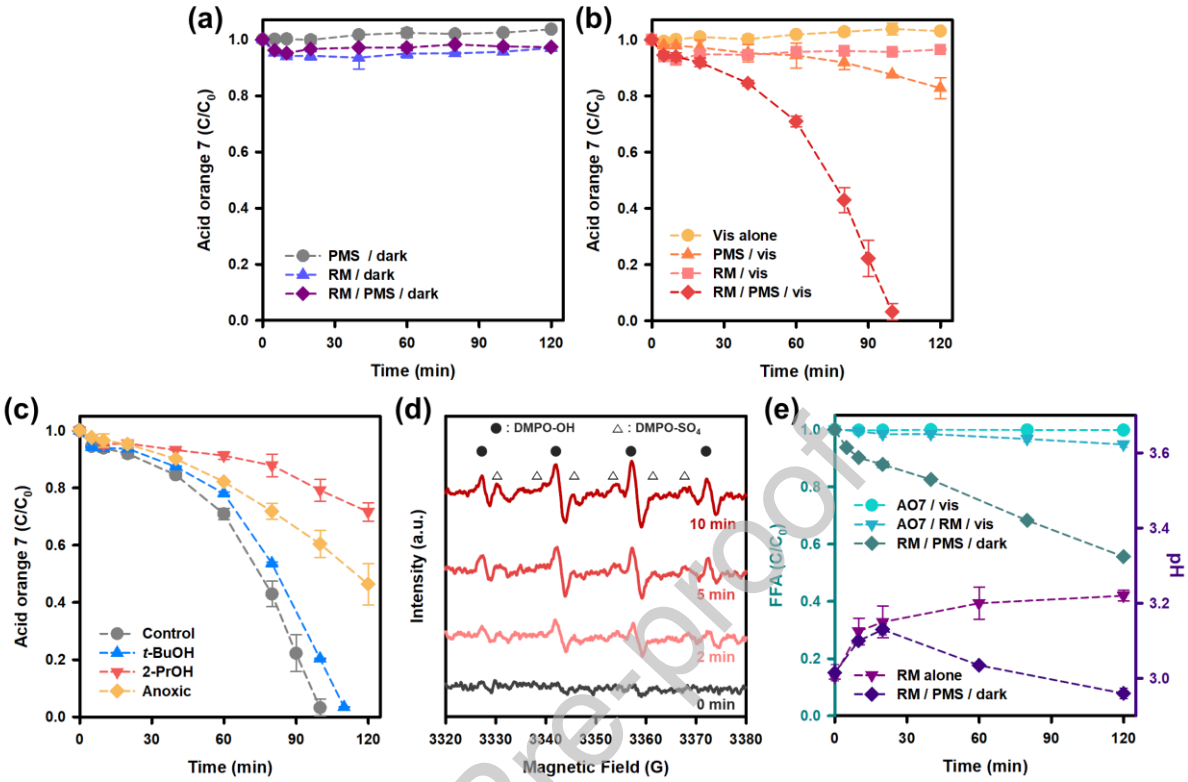

Fig. 2. Degradation kinetics of AO7 (a) in dark conditions and (b) under visible light irradiation; (c) effects of *t*-BuOH, 2-PrOH, and deoxygenation on the degradation of AO7; (d) ESR spectra of DMPO-OH and DMPO-SO_4 adducts obtained by the RM/PMS/vis system in conjunction with AO7; and (e) degradation kinetics of FFA for $^1O_2$ detection and pH variation while mixing the RM suspension in the absence of and presence of PMS. (Conditions: $[RM]_0$ = 0.1 g/L, $[PMS]_0$ = 4 mM, $[AO7]_0$ = $[FFA]_0$ = 0.17 mM, $[t\text{-BuOH}]_0$ = $[2\text{-PrOH}]_0$ = 100 mM, $[DMPO]_0$ = 100 mM, pH_i = 3.0, I = 100 mW/cm^2 ($\lambda > 400$ nm)).

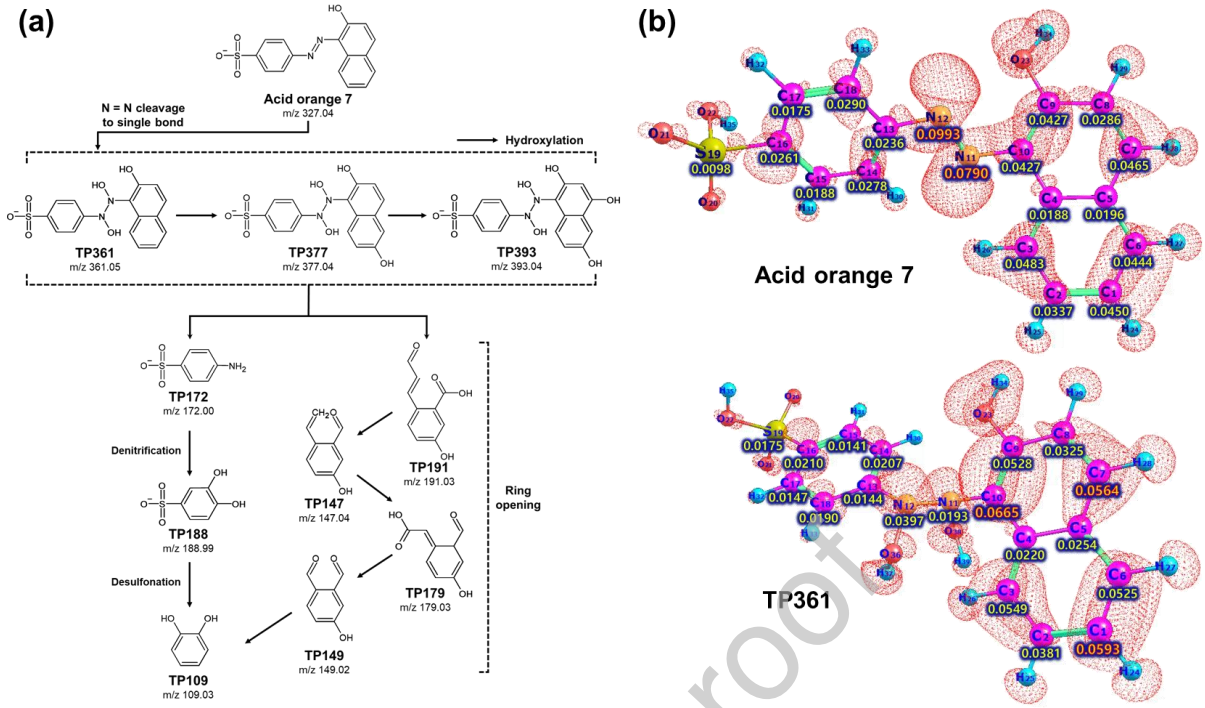

Fig. 3. (a) Pathway for oxidative degradation of AO7 by the RM/PMS/vis system, and (b) condensed Fukui function for electrophilic attack (f^-) on (a) AO7 and TP361.

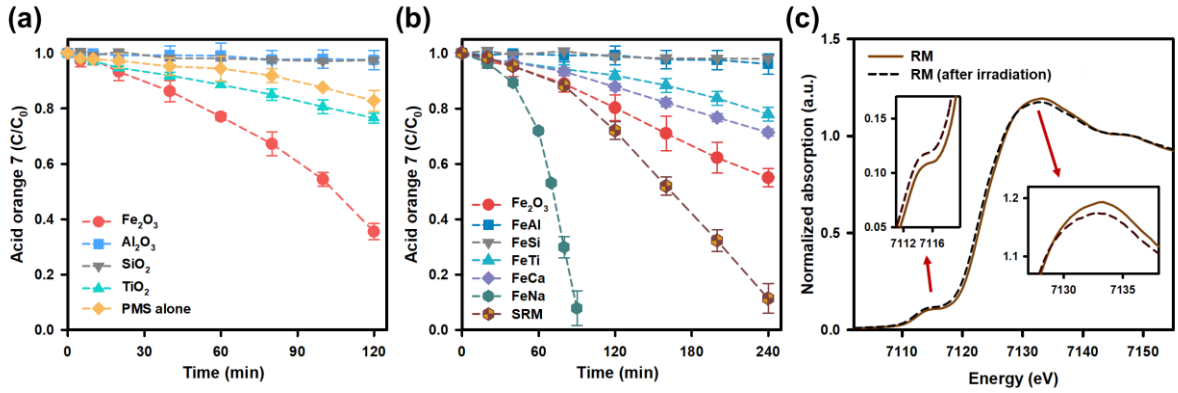

Fig. 4. Degradation kinetics of AO7 (a) using single metal oxides and (b) metal oxide composites with PMS under visible light irradiation; the amount of metal oxide composites contained in 0.1 g/L RM was used; (c) Fe K-edge XANES spectra of pristine RM, and visible light irradiated RM in the presence of AO7. (Conditions: $[\text{catalyst}]_0$ = 0.1 g/L for (a), $[Fe_2O_3]_0$ = 37 mg/L, $[\text{FeAl}]_0$ = 62 mg/L, $[\text{FeSi}]_0$ = 48 mg/L, $[\text{FeTi}]_0$ = 44 mg/L, $[\text{FeCa}]_0$ = 43 mg/L, $[\text{FeNa}]_0$ = 43 mg/L, $[\text{SRM}]_0$ = 89 mg/L for (b), $[\text{PMS}]_0$ = 4 mM, $[\text{AO7}]_0$ = 0.17 mM, pH_i = 3.0, I = 100 mW/cm^2 ($\lambda > 400$ nm)).

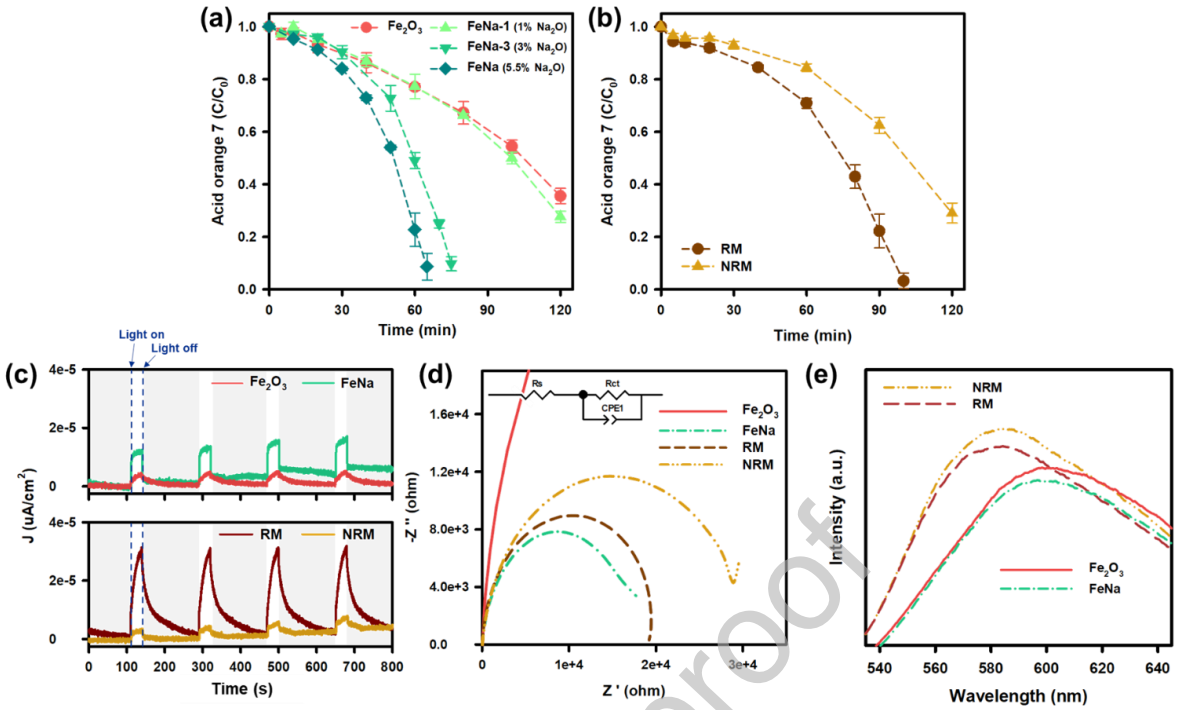

Fig. 5. Degradation kinetics of AO7 using (a) FeNa synthesized in different concentration of Na_2O and (b) neutralized RM with PMS under visible light irradiation; (c) photocurrent density; (d) EIS measurement for Fe_2O_3, FeNa, RM, and NRM in the presence of AO7 and PMS; and (e) PL spectra of Fe_2O_3, FeNa, RM, and NRM in the presence of AO7. (Conditions: $[catalyst]_0$ = 0.1 g/L, $[PMS]_0$ = 4 mM, $[AO7]_0$ = 0.17 mM, $[Na_2SO_4]_0$ = 0.1 M, WE = material-coated ITO, CE = Pt mesh, RE = Ag/AgCl, I = 100 mW/cm^2 ($\lambda > 400$ nm)).

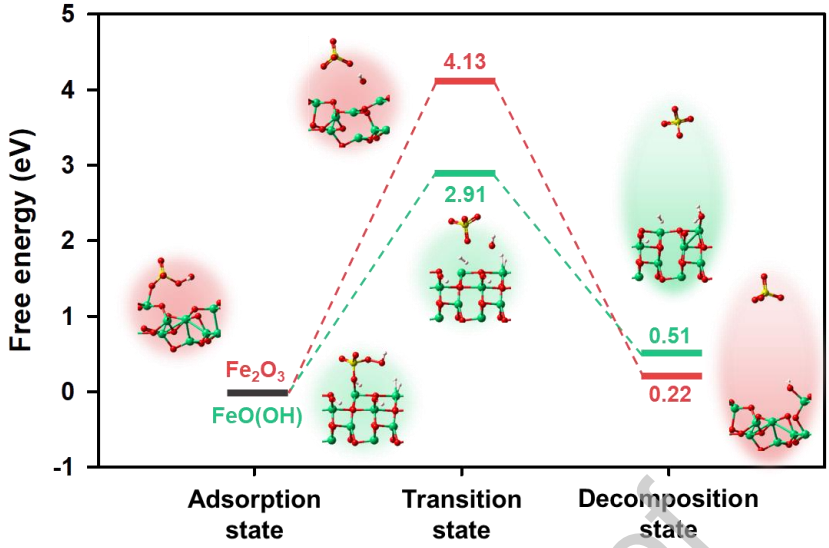

Fig. 6. Energy barriers of radical pathways in Fe_2O_3/PMS and FeO(OH)/PMS systems.

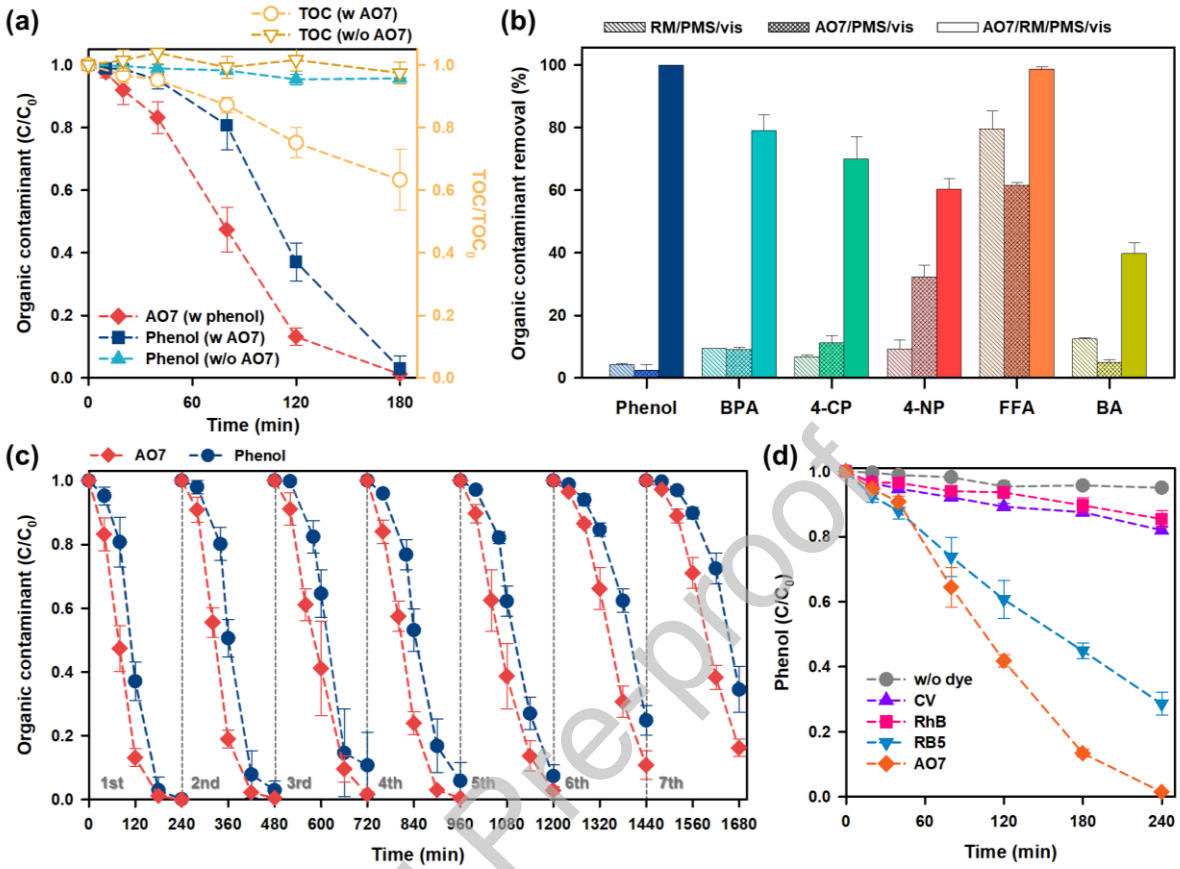

Fig. 7. (a) Oxidative degradation and mineralization kinetics of phenol by RM/PMS/vis and AO7/RM/PMS/vis systems; (b) degradation of various organic contaminants by RM/PMS/vis, AO7/PMS/vis, and AO7/RM/PMS/vis systems for 3 h; (c) simultaneous degradation kinetics of AO7 and phenol by AO7/RM/PMS/vis system during recycling test; and (d) effect of dye type on degradation of phenol by dye-sensitized RM/PMS/vis system. (Conditions: $[RM]_0$ = 0.1 g/L, $[PMS]_0$ = 4 mM, $[Phenol]_0$ = $[BPA]_0$ = $[4\text{-}CP]_0$ = $[4\text{-}NP]_0$ = $[FFA]_0$ = $[BA]_0$ = 0.17 mM, $[AO7]_0$ = 0.17 mM for (a) − (c) and 50 μM for (d), $[CV]_0$ = $[RhB]_0$ = $[RB5]_0$ = 50 μM, pH_i = 3.0, I = 100 mW/cm^2 ($\lambda > 400$ nm)).

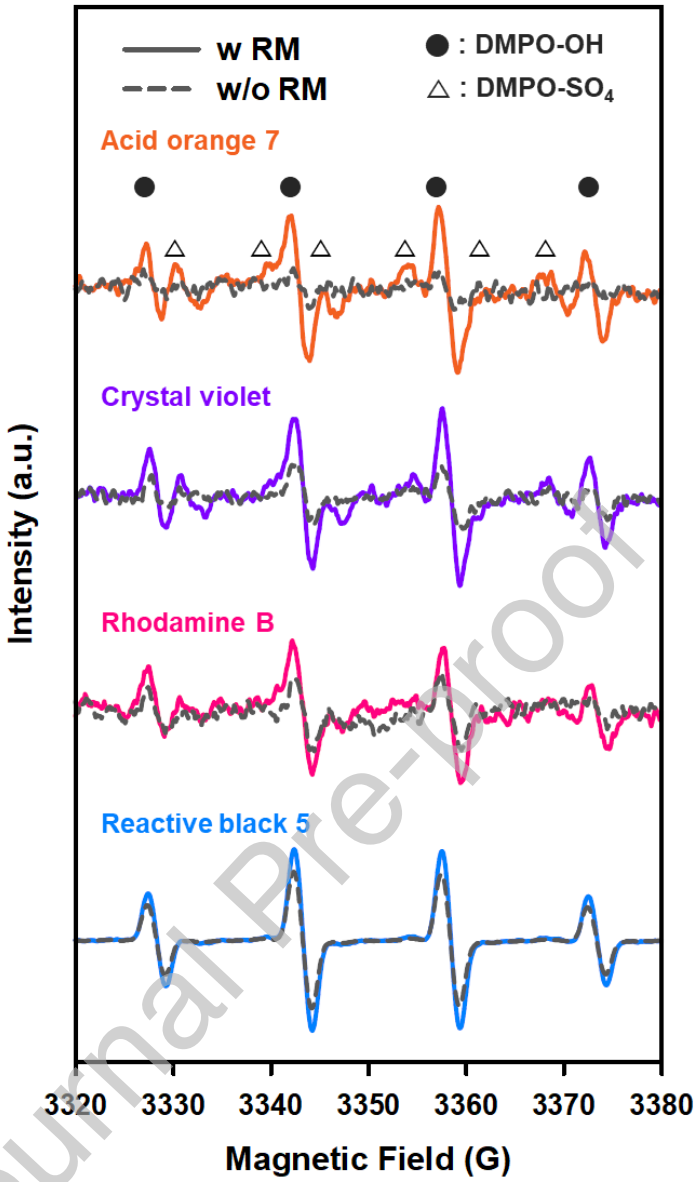

Fig. 8. ESR spectra of DMPO-OH and DMPO-SO_4 adducts obtained by dye/PMS/vis and dye/RM/PMS/vis systems. (Conditions: $[RM]_0$ = 0.1 g/L, $[PMS]_0$ = 4 mM, $[AO7]_0$ = $[CV]_0$ = $[RhB]_0$ = $[RB5]_0$ = 50 μM, $[DMPO]_0$ = 100 mM, pH_i = 3.0, I = 100 mW/cm^2 (λ > 400 nm)).

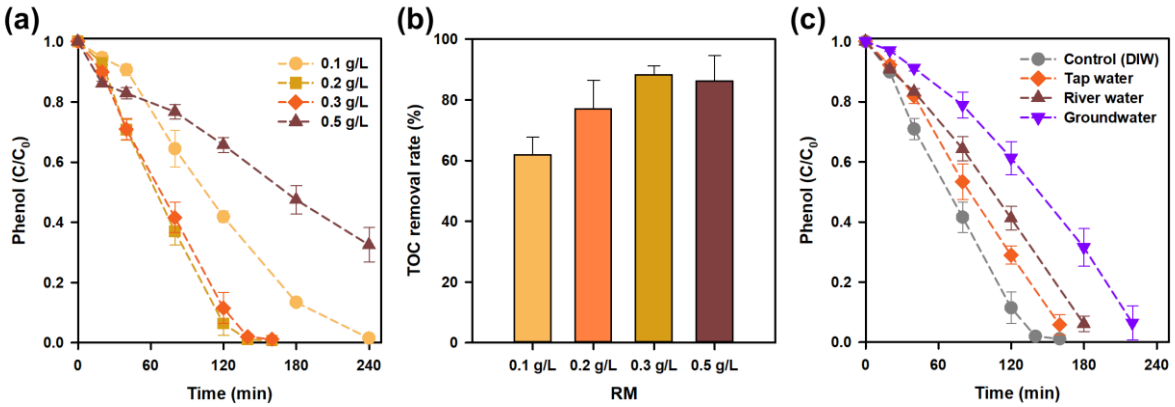

Fig. 9. (a) Degradation kinetics of phenol using different concentrations of RM by the AO7/RM/PMS/vis system for 4 h; (b) TOC removal rate after one-day reaction in the AO7/RM/PMS/vis system using different concentrations of RM; (c) effect of water matrices on phenol degradation by the optimized AO7/RM/PMS/vis system. (Conditions: $[PMS]_0$ = 4 mM, $[AO7]_0$ = 50 μM, $[phenol]_0$ = 0.17 mM, $[RM]_0$ = 0.3 g/L for (c), pH_i = 3.0, I = 100 mW/cm^2 ($\lambda > 400$ nm)).

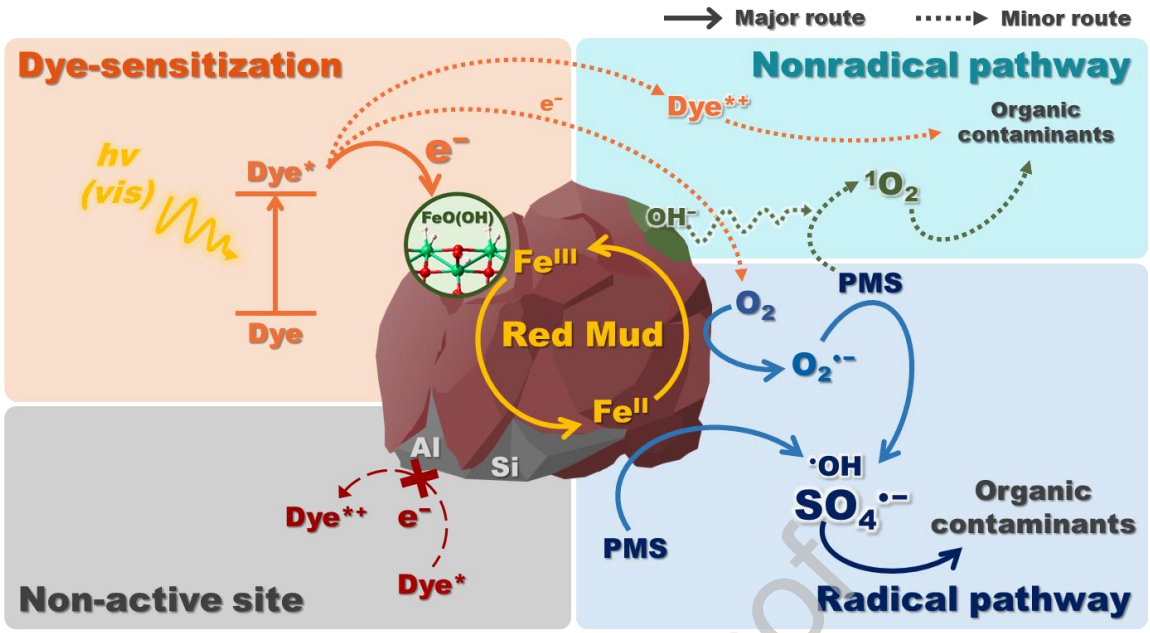

Fig. 10. Proposed mechanism for dye-sensitized oxidation of persistent contaminants by RM/PMS/vis system.

Graphical abstract

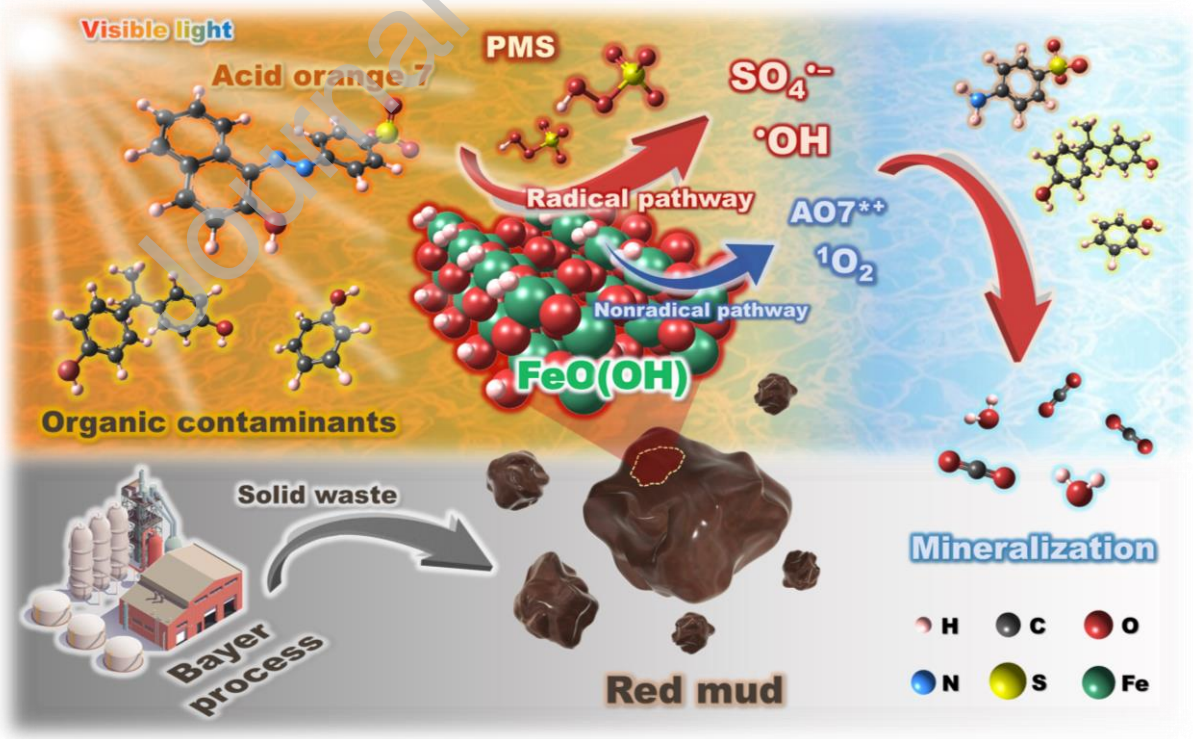

Declaration of interests

☒ The authors declare that they have no known competing financial interests or personal relationships that could have appeared to influence the work reported in this paper.

☐The authors declare the following financial interests/personal relationships which may be considered as potential competing interests: